This manuscript has been submitted for publication in **Marine Pollution Bulletin** journal. Please note that currently manuscript is under review and has yet to be formally accepted for publication. Subsequent versions of this manuscript may have slightly different content. If accepted, the final version of this manuscript will be available via the "Peer-reviewed Publication DOI" link on the right-hand side of this webpage. Please feel free to contact any of the authors; we welcome feedback.

Low Environmental Impact Remediation of Microplastics: Visible-Light Photocatalytic Degradation of PET Microplastics Using Bio-Inspired C,N-TiO_2/SiO_2 Photocatalysts

Maria Camila Ariza-Tarazona[a,b*], Cristina Siligardi[a,b], Hugo Alejandro Carreón-López[c], José Enrique Valdéz-Cerda[c], Paolo Pozzi[a], Garima Kaushik[e] , Juan Francisco Villarreal-Chiu[c,d], Erika Iveth Cedillo-González[a,b*]

[a]Department of Engineering "Enzo Ferrari", University of Modena and Reggio Emilia, Via P. Vivarelli 10/1, Modena, 41125, Italy.

[b]National Interuniversity Consortium of Materials Science and Technology (INSTM), Via Giusti, Florence, 50121, Italy

[c]Universidad Autónoma de Nuevo León, Facultad de Ciencias Químicas. Av. Universidad S/N Ciudad Universitaria, San Nicolás de los Garza, 66455, Nuevo León, México.

[d]Centro de Investigación en Biotecnología y Nanotecnología (CIByN), Facultad de Ciencias Químicas, Universidad Autónoma de Nuevo León. Parque de Investigación e Innovación Tecnológica, Km. 10 autopista al Aeropuerto Internacional Mariano Escobedo, Apodaca, 66628, Nuevo León, México.

[e]Department of Environmental Science, School of Earth Sciences, Central University of Rajasthan, Ajmer 305817, India

[*]***Corresponding authors***

mariacamila.arizatarazona@unimore.it (M. C. Ariza-Tarazona),

ecedillo@unimore.it (E.I. Cedillo-González)

Twitter handles: @cedillo_iveth; @MCamilaAriza

Abstract

Microplastics (MPs) are plastic particles of ≤5 mm with a ubiquitous presence in aquatic ecosystems. MPs harm marine life and can cause severe health problems for humans. Advanced oxidation processes (AOPs) that involve the in-situ generation of highly oxidant hydroxyl radicals can be an alternative to fight MPs pollution. Of all the AOPs, photocatalysis has been proven a clean technology to overcome microplastic pollution. In this work, we propose novel C,N-TiO_2/SiO_2 photocatalysts with proper visible-active properties to degrade polyethylene terephthalate (PET) MPs. Photocatalysis was performed in an aqueous medium and at room temperature, evaluating the influence of two pH values (pH 6 and 8). The obtained results demonstrated the degradation of the PET MPs by C,N-TiO_2/SiO_2 semiconductors and achieved mass loss between 9.35 and 16.22%, carbonyl indexes up to 28.7% lower, and a significant decrease in crystallinity compared to the original PET MPs.

Keywords: PET; photocatalysis; microplastics; C,N-TiO_2/SiO_2; crystallinity; DSC.

1. Introduction

The presence of plastics in the ocean is one of the most pressing environmental issues of the current century. Plastic bags, six-pack rings, or ghost nets cause entanglement and asphyxia of the marine biota. The harmful effects of those and other big plastic items in the marine environment are readily visible. Hence various efforts to combat marine pollution caused by such plastic items are now being implemented worldwide. However, since 2010, the scientific community has started to keep records of the smaller plastic debris, the so-called microplastics (MPs). MPs are plastics with sizes between 1 μm and 5 mm that

were intentionally fabricated in those sizes or that, more often, come from the breakdown of larger plastic items (Wang et al., 2021). Due to their high area-to-volume ratio and surface chemical properties, MPs adsorb persistent organic pollutants (POPs) when they are present in contaminated aquatic environments (Gao et al., 2019). Marine biota frequently consumes MP, which promotes physical damage to their tissues by direct contact (Hale et al., 2020), as well as other general health issues caused when MPs act as POPs vectors in the body (Koelmans et al., 2016). This represents a serious ecological problem as it is well-known that MPs are being transferred through the trophic web. Thus, their presence has recently been confirmed in humans (Ragusa et al., 2021; Schwabl et al., 2019).

Formerly, it was assumed that MPs remain inactive in oceans once released. However, studies revealed that they could be transferred to the atmosphere by sea spray (Allen et al., 2020). MPs are already so ubiquitous that, similar to global biogeochemical cycles, MP now spiral around the globe with different atmospheric, oceanic, cryospheric and terrestrial residence times (Brahney et al., 2021). In terrestrial environments, MPs cause similar damages to those observed in the marine environment. MPs are consumed by terrestrial biota leading to impaired health and mortality, transfer up the trophic web and act as vectors for pollutants (Brahney et al., 2021). Additionally, MPs interfere with soil dynamics and plant production, altering the microbial community's composition. Due to the previous arguments, MPs are considered an emergent pollutant of global concern, and there is an urgent need for technological solutions to solve MP pollution. The ocean now not only acts as a MP’s sink but has already become a source; hence, a logical approach to fight MP pollution is to stop their

79 inputs into the ocean. A feasible and relatively straightforward approach to
80 accomplish this goal is to effectively eliminate the MP present in wastewater
81 effluents before their discharge into water bodies. This approach is based on
82 the fact that wastewater treatment plants (WWTPs) have been identified as a
83 source of MPs in aquatic and terrestrial environments (Barceló and Picó, 2019;
84 Sharma et al., 2020). Photocatalysis is a water treatment process that can be
85 adapted as tertiary treatment into WWTPs. By photocatalysis, MP can be
86 mineralized to CO_2 and H_2O or degraded into less toxic substances (Jiang et
87 al., 2021; Uheida et al., 2021). Furthermore, if performed in visible or solar light
88 and if the photocatalyst is prepared using renewable feedstocks, the overall
89 process respects the 6^{th}, 7^{th}, and 9^{th} principles of Green Chemistry (Jiménez-
90 González and Constable, 2011).
91 Even though all types of plastics have been found in the marine environment,
92 polyethylene terephthalate (PET) is prevalent in many ecosystems due to its
93 extended use and particular properties. PET is a thermoplastic polyester
94 composed of glycolate and terephthalate subunits connected by ester bonds
95 (Zhang et al., 2021). Together with polypropylene, they represent 26.7% of
96 worldwide plastic demand (Magalhães et al., 2020), and their applications
97 include bottles for drinking and cleaning products and polyester fibers used in
98 clothing. PET is predominantly found in deep sea and sewage works because
99 of its high density compared to other plastics (1.36-1.37 g/cm^3) (Bond et al.,
100 2018) and its high resistance to biodegradation (Mueller, 2006). Hence, this
101 research attempts to degrade this pollutant through photochemical methods and
102 analyze the efficacy of the process through various characterization studies.

The photocatalytic degradation of PET in an aquatic environment involves two main mechanisms: photo-oxidation and hydrolysis. The hydrolytic degradation of PET strongly depends on the pH and temperature of the surrounding medium (Nguyen-Tri et al., 2014). Even though PET has heteroatoms in the backbone, which are highly susceptible to hydrolysis, the presence of aromatic groups makes PET highly resistant to degradation under normal conditions (Niaounakis et al., 2019). Because of this, PET hydrolysis is relatively slow, especially at a pH of around 7 (Chamas et al., 2020; Ioakeimidis et al., 2016; Nguyen-Tri and Prud'homme, 2019). Even though the mechanism for hydrolytic degradation is not fully understood (Fotopoulou and Karapanagioti, 2017), it has been reported that in an acidic or alkaline environment, the rate of hydrolysis has a substantial increase (Allen et al., 1994; Edge et al., 1991). In an acidic environment, the protonation of the oxygen atom of the ester group reacts with water to produce hydroxyl and carboxyl end-groups (Allen et al., 1994). In an alkaline environment, the hydroxide anion attacks the carboxyl oxygen atom, producing hydroxyl and carboxyl end-groups (Edge et al., 1991). In this work, the photocatalytic degradation of PET MPs was tested under ambient temperature and two pH, one slightly acidic at pH 6 and the other slightly alkaline at pH 8, to be closer to natural conditions while also promoting the hydrolytic degradation at non-neutral pH values.

1. Materials and methods

1.1. C,N-TiO_2/SiO_2 synthesis and characterization

Two C,N-TiO_2/SiO_2 photocatalysts were synthesized using the extrapallial fluid (EPF) of two different mussel species. According to Zeng *et al.* (2015), the EPF of mussels contains proteins that can be used as doping sources (C and N) and

129 pore-forming templates. One photocatalyst C,N-TiO_2/SiO_2, was synthesized
130 using *Mytilus Edulis* mussels fluid, referred to as TS-ME, and the other using
131 *Mytilus Galloprovincialis* mussels fluid, which will be referred to as TS-MG in
132 this manuscript. The synthesis consisted of two main procedures. The first one
133 is a modification from the procedure proposed by Zeng *et al.* (2015) (Zeng et
134 al., 2015), who intended to obtain a C,N-TiO_2 semiconductor. The methods for
135 extracting the extrapallial fluid and the synthesis process are already described
136 in detail in our previous work (Ariza-Tarazona et al., 2020). Briefly, 5 mL of
137 titanium butoxide and 25 mL of extrapallial fluid of *Mytilus edulis* or *Mytilus*
138 *Galloprovincialis* mussels were mixed in a beaker and kept under stirring for 2
139 h. Then, the mixture was left to mineralize for 4 h without stirring. The second
140 procedure intends to couple the C,N-TiO_2 photocatalyst with SiO_2. In another
141 beaker, 2 mL of tetraethyl orthosilicate and 3.2 mL of isopropyl alcohol were
142 mixed and kept under stirring for 15 minutes. After that, 0.8 mL of distilled water
143 and 0.10 mL of concentrated nitric acid were added, and the solution was
144 stirred for another 2 h. Further, the contents of both beakers were mixed and
145 stirred for 20 min. The homogeneous mixture was transferred to an autoclave
146 and subjected to a thermal treatment as described in our previous work (Ariza-
147 Tarazona et al., 2020).
148 The crystalline structure of the photocatalysts was investigated by X-ray
149 diffraction (XRD), using a Siemens D5000 diffractometer with Cu Kα radiation
150 (accelerating voltage of 40 kV, current of 40 mA, and 2θ-step of 0.023°). The
151 scan was collected between 5 and 80 degrees. The functional groups at the
152 photocatalysts' surface were detected with attenuated total Reflectance-Fourier
153 transform infrared (ATR-FTIR) spectroscopy. The ATR-FTIR spectra were

collected using a Vertex 70 ATR-FTIR Bruker spectrometer by averaging 32 scans between 4000 and 400 cm^{-1} with a 4 cm^{-1} spectral resolution. The surface area was estimated by nitrogen adsorption using a Micromeritics TriStar II Plus 3.01 surface area analyzer (analysis bath temperature of 77.3 K, equilibration interval of 5 s, and degasification at 110 °C). The photocatalysts' band gap (E_g) values were calculated from their Diffuse reflectance spectra (DRS). Measures were carried out in the 300–800 nm range on a Jasco V-670 UV–Vis/NIR spectrophotometer equipped with an ILN-725 integration sphere. X-ray photoelectron spectroscopy (XPS) was used to investigate the surface chemistry of the photocatalysts. XPS analyses were carried out using a Thermo Scientific Escalab 250Xi, maintaining a base analysis pressure of ~10-10 mbar; the excitation of the analyzed photoelectrons was performed with a monochromatic X-ray source of Al Kα (1486.68 eV) with a analysis area radius of 650μm. The analysis conditions for the high-resolution zones were step energy of 20 eV and 45° take-off angle with a step of 0.1eV. Microstructural characterization was carried out by field emission gun scanning electron microscopy (FEG-SEM) using an FEI Nova Nano SEM 450 instrument.

1.2. PET MPs preparation and characterization

Secondary PET MPs were obtained by grinding a PET food container with a coffee grinder. These particles were then sifted to obtain particles of size ≤500 μm. Their size and morphology were analyzed by optical microscopy (OM) using a Leica EZ4 stereomicroscope. To determine the type of polymer present in the sample, an attenuated total reflectance Fourier transformed infrared spectroscopy (ATR-FTIR) in a Vertex 70 ATR-FTIR Bruker spectrometer was used.

1.3. Photocatalytic degradation experiments

Photocatalytic degradation experiments were performed at room temperature in a closed reaction chamber, where a 50W LED visible light lamp illuminated the sample from the top. The sample consisted of a Batch-type glass container containing 200 mg of PET microplastics and 200 mg of TS-ME or TS-MG in 50 mL of buffer solution of pH 6 or 8. The light irradiance of the lamp was 500 W/m^2 throughout the experiments. The solution was kept under continuous stirring at 350 rpm for 120 h of irradiation. After irradiation, the solution was filtered with a Whatman 40 filter, dried at room temperature for 12 h, and then incubated at 50 °C for 2 h in an oven. The heterogeneous mixture of photocatalyst/PET microplastics was weighed, and the weight of the semiconductor was extracted to obtain the remanent weight of the microplastics. The photolysis tests followed the same process without the photocatalysts. The degradation was followed by measuring the % of mass loss of the PET microplastics according to the following equation:

$$\%\ Mass\ loss = \frac{Initial\ mass\ of\ PET\ MPs - Mass\ of\ PET\ MPs\ at\ 120\ h}{Initial\ mass\ of\ PET\ MPs}\ x\ 100 \quad \text{(Eq.1)}$$

ATR-FTIR analysis was used to determine the photocatalytic degradation by identifying functional groups formed after 120 h of visible light irradiation. The carbonyl index (CI) was used to assess the degradation of PET MPs. According to the literature, CI was calculated by dividing the absorption of the carbonyl peak (1710 cm^{-1}) by the absorption of the reference band. Reference bands for PET were read at 1504 cm^{-1}, which corresponds to the aromatic ring C=C bond (Piccardo et al., 2020), and at 871 cm^{-1}, which corresponds to the C-H vibrations of the aromatic ring (Janczak et al., 2020).

The crystallinity of PET MPs was studied by Differential scanning calorimetry (DSC) to detect alterations in the PET macromolecule because of photocatalytic degradation. The analysis was carried out in a TA Instruments DSC 2010 Differential Scanning Calorimeter in a nitrogen atmosphere. The temperature ranged from 20 to 300 °C with a heating rate of 10 °C/min. The glass transition (T_g), cold crystallization (T_{cc}), and melting temperatures (T_m) were determined. The T_g was obtained at the inflexion point of the heat capacity. The exothermic peak minimum and endothermic peak maximum correspond to T_{cc} and T_m, respectively. The cold crystallization and melting enthalpies were obtained from the area under the curve of their corresponding peaks. The degree of crystallinity (X_c) during the DSC heating stage of the PET MPs was calculated according to the following equation (Mendiburu-Valor et al., 2022):

$$Xc = \frac{\Delta H_m - \Delta H_{cc}}{\Delta H_0} \, x \, 100 \qquad \text{(Eq.2)}$$

Where X_c is the degree of crystallinity (%), ΔH_m is the melting enthalpy (J/g), ΔH_{cc} is the cold crystallization enthalpy (J/g), and ΔH_0 is the melting enthalpy for a 100% crystalline PET (140 J/g) (Loaeza et al., 2021).

The thermal behavior of PET MPs before and after photocatalytic degradation was investigated by thermogravimetric analysis (TGA). TGA measurements were performed in an STA 429 CD Simultaneous thermal analyzer. The measurement temperature range was 50–600 °C, the heating rate was 10 °C/min, and the mass of the samples was around 15 mg. The tests were performed in a helium atmosphere at 50 ml/min.

2. Results and discussion

2.1. C,N-TiO_2/SiO_2 Characterization

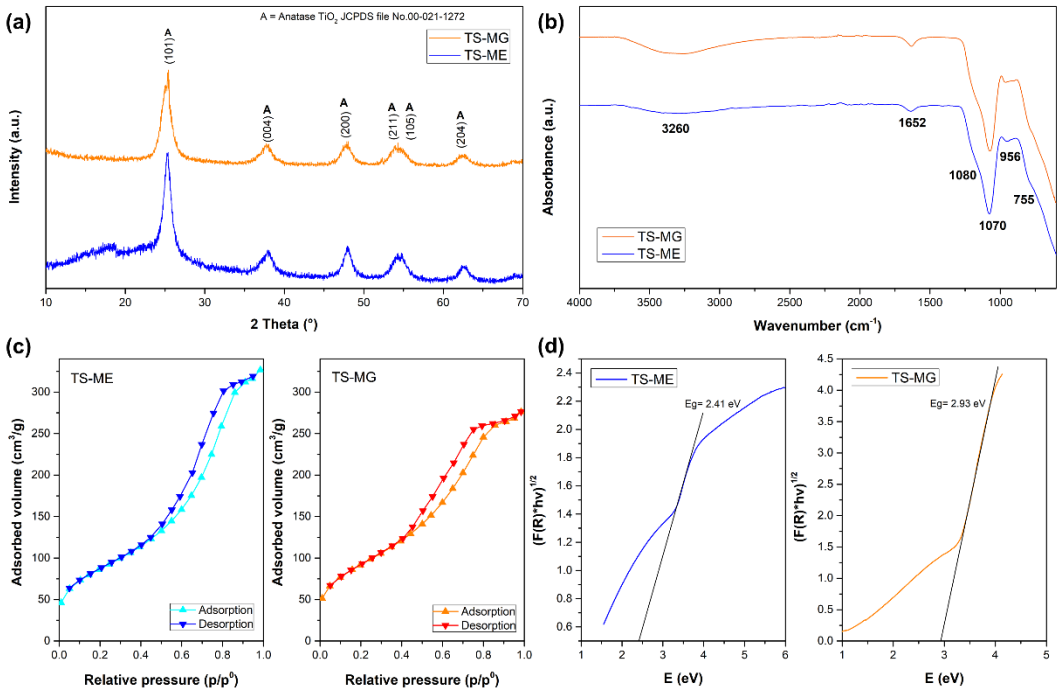

Figure 1. (a) XRD patterns, (b) FTIR-ATR spectra, (c) nitrogen adsorption isotherms, and (d) Eg calculation for TS-MG and TS-ME samples.

Figure 1(a) shows the XRD patterns for the C,N-TiO_2/SiO_2 powders. All the peaks correspond to the anatase TiO_2 and are in accordance with the JCPDS file No. 00-021-1272. The incorporation of EPF proteins in the synthesis makes the materials amorphous, as reported earlier (Ariza-Tarazona et al., 2020, 2019; Zeng et al., 2015). It can be noted that the crystalline structure of TiO_2 is not affected by the incorporation of SiO_2, as the last is in a lower percentage than the detection limit of the instrument, and SiO_2 possibly exists in an amorphous state (Zhang et al., 2019). The FTIR spectrum of the sample is shown in Figure 1(b). The absorption peaks at 755 and 438 cm^{-1} were attributed to Ti–O and Ti–

O–Ti bonds. The broad band at 3500–3200 cm^{-1} was assigned to the stretching vibrations of hydroxyl groups and the bending vibration of the adsorbed H_2O. The absorption peak around 1652 cm^{-1} was referred to the O–H and N–H bonds. The presence of Si in the samples is confirmed by the characteristic peak at 1070 cm^{-1}, attributed to the antisymmetric stretching vibration of the Si–O–Si bond (Zhang et al., 2019). It is also possible that this band overlaps with the band at 1080 cm^{-1}, corresponding to the Ti–N bond. FTIR spectroscopy also detected the symmetric stretching vibration of the Ti-O-Si bond at 956 cm^{-1}. It has been reported that the existence of this bond can improve the photocatalytic activity of the semiconductor since it may lead to the increase of surface defects, resulting in a higher capture of photogenerated carriers and an enhanced activity of the hydroxyl radical (Guo et al., 2014).

Table 1. Properties of the C,N-TiO_2/SiO_2 photocatalysts using the extrapallial fluid of different species of mussels as a doping source.

Sample	E_g (Ev)	Activation wavelength (nm)	S_{BET} (m^2/g)
TS-ME	2.41	514	313
TS-MG	2.93	423	332

The properties of the C,N-TiO_2/SiO_2 photocatalysts are presented in Table 1. The optical properties of the photocatalyst were investigated by UV-Vis diffuse reflectance spectroscopy. The absorbance spectrum is shown in Figure 1S (Supplementary material). Using the Kubelka-Munk theory, the E_g values were obtained from the intersection of a straight line from the linear region with the abscissa axis of a plot the $[F(R)hv]^{1/2}$ vs. E. The bandgap energy was found to

266 be 2.41 eV and 2.93 for TS-ME and TS-MG, respectively. This result suggests
267 that C,N-TiO_2/SiO_2 could have an enhanced photocatalytic activity under visible
268 light.
269 The N_2 adsorption-desorption isotherm is presented in Figure 1(d). The samples
270 showed a type IV isotherm according to IUPAC, characteristic of mesoporous
271 materials. The hysteresis loop was attributed to H1, indicating that the
272 semiconductor is composed of agglomerates of spherical particles. These
273 textural properties of the material explain the high obtained BET surface area of
274 313 m^2/g for TS-ME and 332 mg^2/g for TS-MG. Zeng et al. (Zeng et al., 2015)
275 synthesized different N-TiO_2 photocatalysts using different concentrations of
276 EPF-derived proteins. Among them, the one with the best physical properties
277 had a 1200 µg/mL concentration. This material had a surface area value three
278 times that of Degussa P25, indicating the positive effect of implementing the
279 EPF from mussels. As they stated, the proteins in this fluid form a 3D network
280 with sites or channels where TiO_2 nuclei can be generated after being mixed
281 with the TiO_2 precursor (titanium tetrabutoxide) and then kept at rest for 4 h.
282 After being subjected to thermal treatment, the proteins were removed, leaving
283 a porous structure of N-TiO_2 with a high surface area. For the C,N-TiO_2 material
284 that was synthesized in our previous work using *Mytilus Edulis* mussels (Ariza-
285 Tarazona et al., 2020), the superficial area value is four times than the one of
286 Degussa P25, while for the C,N-TiO_2/SiO_2 synthesized in this work is up to five
287 times the superficial area of Degussa P25. The differences in the increase in
288 surface area between the semiconductors synthesized using *Mytilus Edulis* (TS-
289 ME) and *Mytilus Galloprovincialis* (TS-MG) mussels and the semiconductor

290 synthesized by Zeng et al. (Zeng et al., 2015) can be attributed to the different
291 properties of the species of mussels used.
292 The photocatalyst surface was also analyzed using X-ray photoelectron
293 spectroscopy (XPS). The XPS survey in Figures 2(a) and 2(e) confirms the
294 presence of O, Ti, Si, N, and C elements. The O 1s spectrum exhibits two
295 peaks for TS-ME (Figure 2(b) and one peak for TS-MG (Figure 2(h)). The peak
296 at 532.96 eV may be attributed to Ti-O-Si species (Aman et al., 2016) that had
297 been already identified according to the FT-IR spectrum of the sample, while
298 the peaks at around 530 eV are ascribed to the O in the Ti-O-Ti lattice. The
299 spectrum for Ti 2p presents two peaks at around 458 and 464 eV for both
300 samples, corresponding to Ti $2p_{3/2}$ and Ti $2p_{1/2}$, respectively (Zeng et al., 2015).
301 N 1s XPS spectra of TS-ME (Figure 2b) show a broad peak at 400 eV,
302 suggesting an interstitial nitrogen dopant (Ang et al., 2009), while for TS-MG
303 (Figure 2(f)), an N 1s peak is detected at 396 eV, suggesting that the nitrogen is
304 found in a substitutional position (Zeng et al., 2015). In the spectrum of C
305 element, for TS-ME (Figure 2(c)), two peaks were identified at 288.75 and
306 284.88 eV, which are attributed to sp2 hybridization in CNOs or C of Ti–O–C
307 bonds and the C=O in CNOs, respectively (Zhang et al., 2019), while TS-MG
308 (Figure 2(g)) presents a broad peak from 288.80 eV to 285.26 eV, suggesting
309 the two peaks mentioned above are overlapped. In the XPS spectrum of Si 2p
310 for both samples (Figure 2(d) and 2(h)), one peak was observed at around 103
311 eV, which may be attributed to Si-O-Si (Zhang et al., 2019).

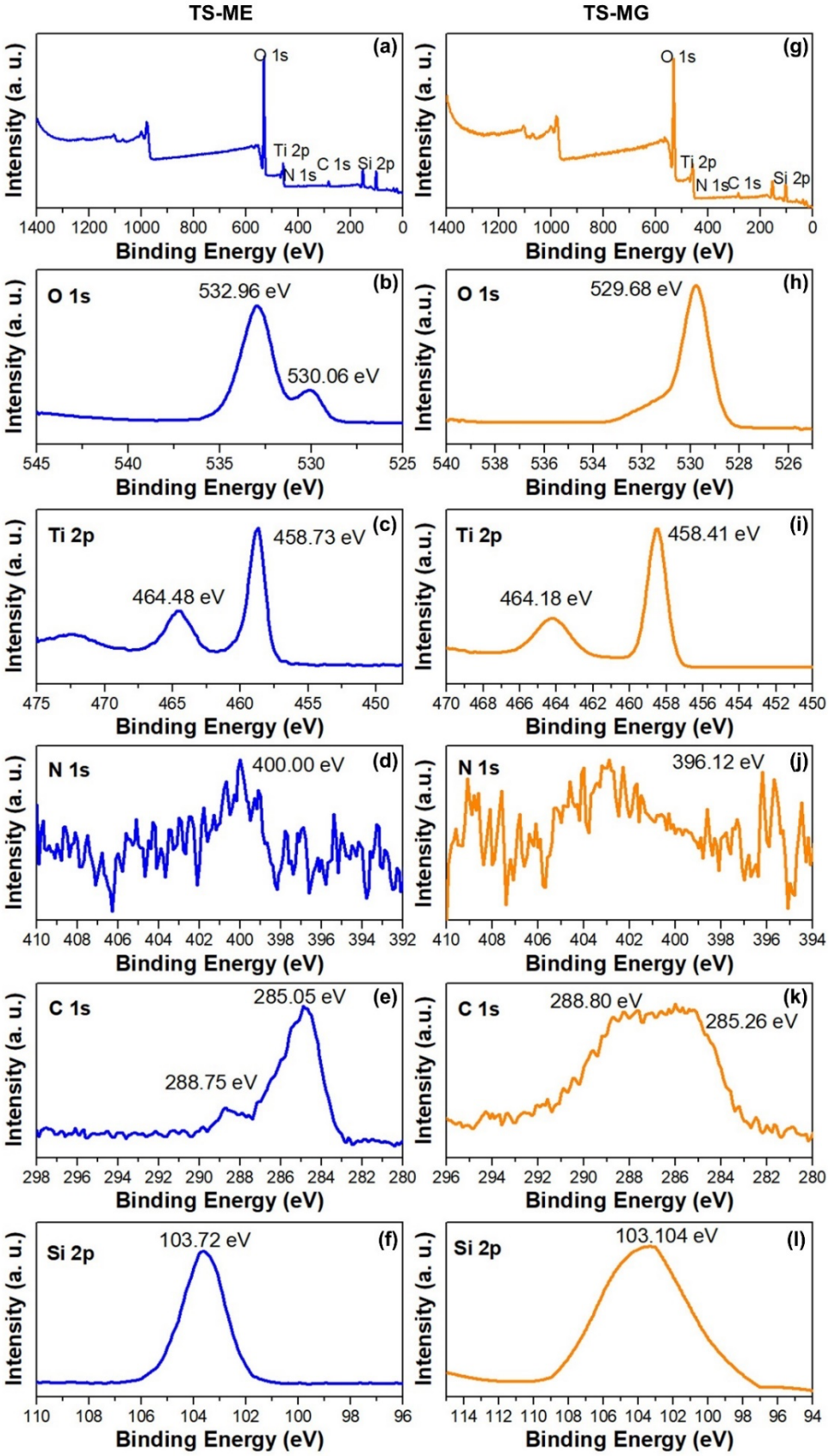

312

313 **Figure 2.** XPS spectra of TS-ME ((a)-(f)) and TS-MG ((g)-(l)): (a), (g) the survey

314 XPS spectra; (b), (h) O 1s; (d), (j) Ti 2p; (e), (k) C 1s; (f), (l) Si 2p.

FEG-SEM micrographs for both photocatalysts are presented in Figure 3. It can be noted that the photocatalysts are composed of two phases. The first is a 3D network (Figure 3(a)-(b) and Figure 3(e)-(f)) of TiO_2, in which the proteins served as templates to generate porosity. The second one is formed by agglomerates of spherical particles that also contribute to increasing the porosity of the C,N-TiO_2/SiO_2 photocatalyst. From Figure 3, it can be inferred that the 3D network is composed of macropores of diameters between 0.5 – 1.6 µm. In addition, the materials also exhibit agglomerates of 1-3 µm constituted of spherical particles with an average radius of 20-50 nm.

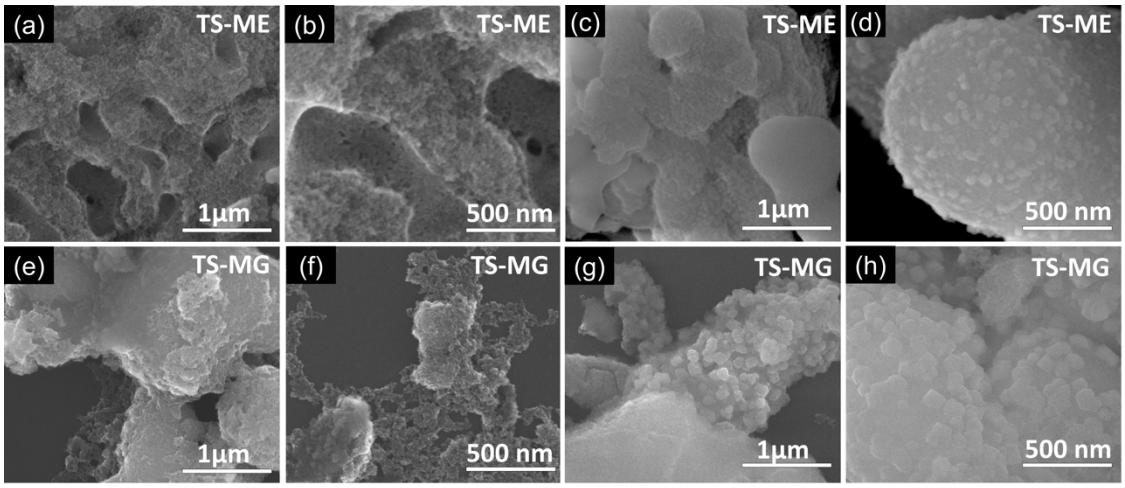

Fig. 3. FEG-SEM micrographs of TS-ME ((a)-(d)) and TS-MG ((e)-(h)) photocatalysts.

3.3. MPs characterization

The original food container used to obtain the MPs and the characterization of the samples of microplastics obtained after grinding are presented in Figure 4. The optical microscopy in Figure 4(b) shows that the sample comprises approximately 200-500 µm sharp microplastic fragments. Figure 4(c) presents the FTIR spectrum of the obtained fragments. The sample presents all main

characteristic bands of PET according to the literature (Piccardo et al., 2020). The band located at 2953 cm^{-1} is assigned to the C-H asymmetric stretching vibrations, while the following bands at 2917 and 2846 cm^{-1} are attributed to the asymmetrical and symmetrical vibrations of CH_2, respectively (Aljoumaa and Abboudi, 2016). The absorption band at 1713 cm^{-1} corresponds to the C=O stretch vibration of the carboxylic ester group, the bands around 1238 to 1092 cm^{-1} are attributed to C-O stretch vibrations, while the bands at 872 and 720 cm^{-1} correspond to the aromatic CH out-of-plane bend (Mendiburu-Valor et al., 2022)

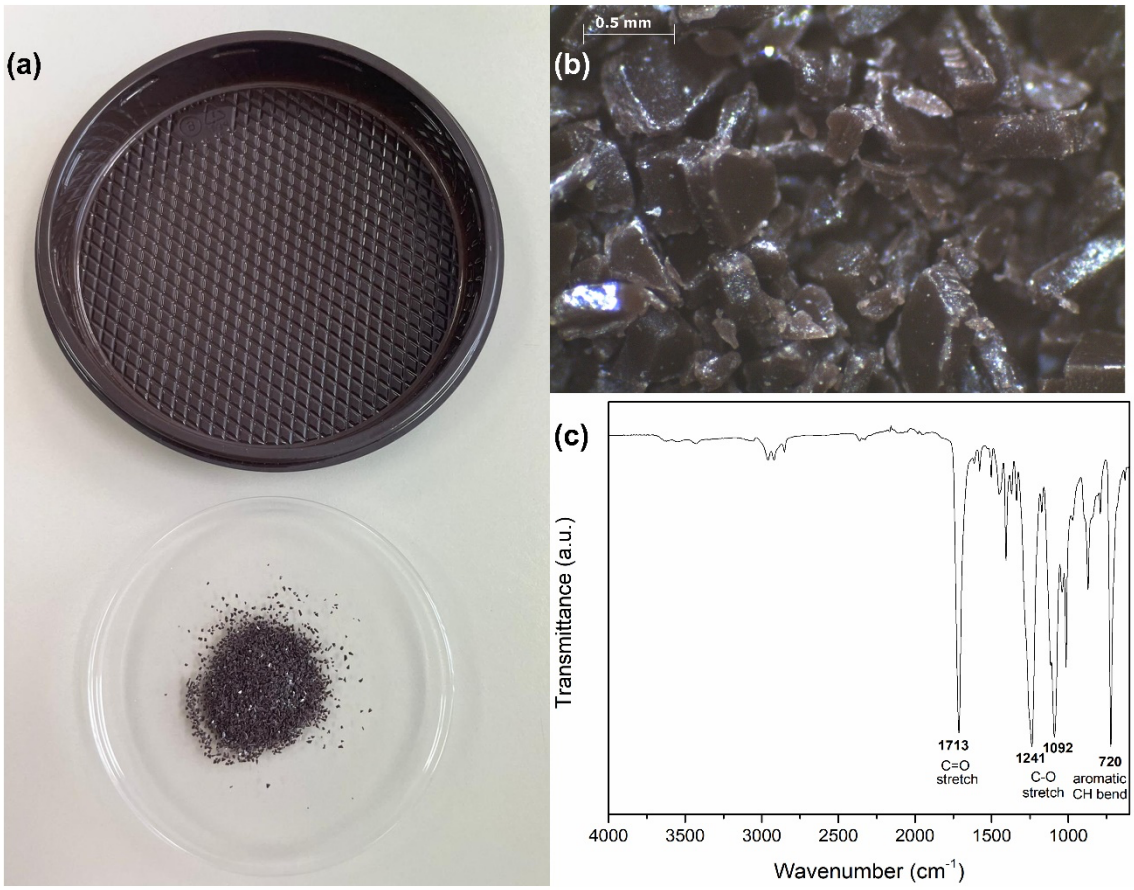

Figure 4. (a) Original PET container, (b) Optical microscopy, and (c) FTIR spectrum of PET MPs.

3.4. Photocatalytic degradation tests

The mass loss of PET samples after photocatalysis and photolysis tests with the calculation of the carbonyl index are presented in Table 2. The mass loss obtained after 120 h of visible light irradiation indicates that the C,N-TiO_2/SiO_2 photocatalysts can degrade PET microplastics at room temperature and pH 6 or 8, achieving mass loss values ranging from 9.35 to 16.22%. Meanwhile, it was proven that the experiments' conditions do not influence the % of mass loss according to the photolysis experiments. Zhou *et al.* (Zhou et al., 2022b) obtained a 10.23% degradation of PET fiber-based MPs under AM 1.5 irradiation for 48 h. However, a slightly more alkaline pH of 9 was necessary. In another work, Zhou *et al.* (Zhou et al., 2022a) reported an approximate 29% mass loss of PET fiber-based MPs under AM 1.5 irradiation for 48 h. Nonetheless, a hydrothermal pretreatment at 180 °C for 12 h was necessary to induce the initial rough appearance and molecular weight reduction.

The analysis of the bands in the FTIR-ATR spectrum is generally used to study PET degradation as it allows monitoring of chemical changes even at the early stages of degradation (Ferreira et al., 2021). Figure 5(a) shows the carbonyl band, while Figure 5(b) shows the spectra from 1500 cm^{-1} to 700 cm^{-1} of PET MPs before and after photocatalytic degradation. The decrease of the band at 1714 cm^{-1} shown in Figure 5a demonstrated the chain scission of the ester group because of photocatalytic degradation. Figure 5(b) presents the ATR-FTIR spectra of original and degraded PET samples from 1500 to 700 cm^{-1}. The bands at 1453 and 1407 cm^{-1} are associated with the C-H deformation and the vibration of the phenylene ring, respectively (Aljoumaa and Abboudi, 2016). The bands at 1370 and 1340 cm^{-1} refer to C-H crystalline *gauche* and *trans* conformations, respectively. Meanwhile, the band at 1238 cm^{-1} is designated for

374 asymmetric C-C-O stretching (Mendiburu-Valor et al., 2022). A band at 1220
375 cm^{-1} developed after irradiation and is associated with the carboxylic acid dimer,
376 as also reported by Horne *et al.* (Horne et al., 2020). Meanwhile, the bands at
377 1117 and 1092 cm^{-1} correspond to the *gauche* and *trans* conformation of the
378 ester C-O-C stretching, respectively (Aljoumaa and Abboudi, 2016). A decrease
379 in the bands at 1238 and 1092 cm^{-1} correlated with C-O degradation (Piccardo
380 et al., 2020). Furthermore, the band at 1015 cm^{-1}, which is attributed to the in-
381 plane bending of C-H in the benzene ring, is also directly related to PET
382 crystallinity, according to literature (Bertoldo et al., 2010; Cole et al., 2002). The
383 bands at 970 and 898 cm^{-1} correspond to the C-H bond stretching of the *trans*
384 and *cis* isomers, respectively (Horne et al., 2020). The bands around 872 and
385 725 cm^{-1} are attributed to the aromatic C-H out-of-plane bending and wagging
386 (Aljoumaa and Abboudi, 2016). However, there is no development of new
387 bands in the stretching vibration of the hydroxyl group or in the region
388 associated with the O-H stretching vibration of ethylene end groups (3615-3115
389 cm^{-1}), as presented in Figure 2S. The development of these bands is
390 associated with the formation of carboxylic and alcoholic end groups due to the
391 photochemical and hydrolytic degradation of the polymer (Ioakeimidis et al.,
392 2016; Mendiburu-Valor et al., 2022; Miranda et al., 2021). Also, at later stages
393 of degradation, additional bands start to form in the region from 1705 to 1685
394 cm^{-1} assigned to the formation of a carboxylic acid dimer, end groups,
395 terephthalic acid monomer, and quinone species (Horne et al., 2020). This
396 indicates that after 120 h of visible light irradiation, the PET samples are in the
397 early stages of degradation.

The carbonyl index, an indicator of the degree of MPs' degradation, tends to reduce as the carbonyl band at 1714 cm^{-1} decreases after 120 h of photocatalytic degradation when 1504 cm^{-1} and 871 cm^{-1} are set as reference bands. When using 1504 cm^{-1} as a reference band, it can be noted that the CI values of all samples are up to 10% lower than the PET original except for PET, TS-MG/pH. This could be attributed to this method's limitations in detecting the degradation of polymers at the early stages of degradation (Rouillon et al., 2016). However, when using 871 cm^{-1} as a reference band, the CI values of the irradiated samples are 12 to 25% lower than the original PET sample, according to the mass loss results obtained.

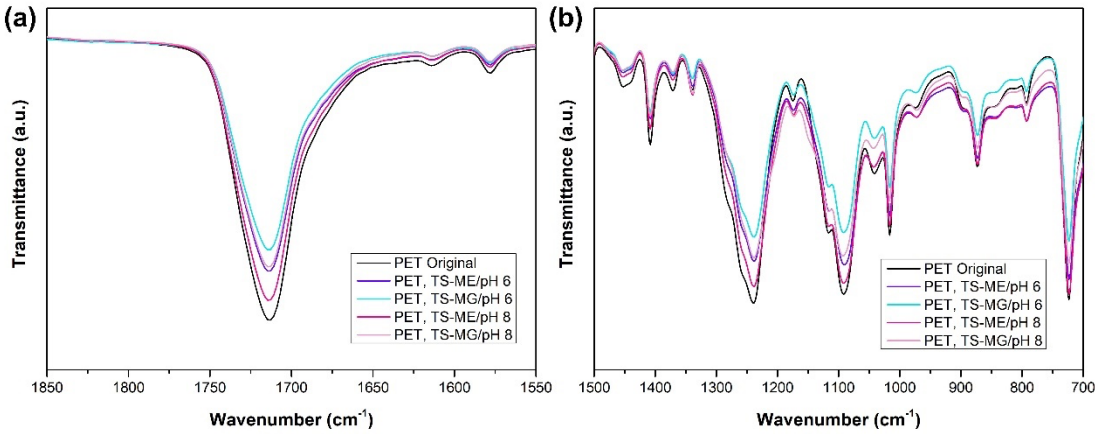

Figure 5. FTIR-ATR spectra of original PET MPs in the regions between (a) 1850-1550 cm^{-1} (carbonyl region) and (b) 1500 - 700 cm^{-1}.

Table 2.% of mass loss and CI calculation for PET samples

Sample	Mass loss (%)	CI(A1714/A1504) (Piccardo et al., 2020)	CI(A1714/A871) (Janczak et al., 2020)
PET Original	-	14.12	3.00
PET, TS-ME/pH 6	13.65 ± 0.90	12.77	2.49
PET, TS-MG/pH 6	16.22 ± 7.52	13.86	2.24
PET, TS-ME/ pH 8	9.35 ± 0.24	13.98	2.43
PET, TS-MG/ pH 8	13.83 ± 0.55	15.05	2.62
PET, Photolysis/pH 6	0.27 ± 0.31	-	-
PET, Photolysis/ pH 8	1.39 ± 0.47	-	-

DSC analysis was used to investigate the response of PET MPs to heating before and after photocatalytic degradation. In particular, the glass transition temperature (T_g), the cold crystallization temperature (T_{cc}), and the melting temperature were obtained for the heating stage. In contrast, the crystallization temperature (T_c) was obtained for the cooling stage. In addition, PET MPs' degree of crystallinity (X_c) was also determined for both stages as it can give information on a polymer's mechanical properties, stability, and chemical resistance (Kong and Hay, 2002).

The heating stage of DSC analysis for PET MPs is presented in Figure 6(a). As can be noted, there are differences in the values of the glass transition temperature (T_g), the cold crystallization temperature (T_{cc}), and the melting temperature (T_m) (values are displayed in Table 3. According to Figure 6(a), the T_g values of PET MPs after photocatalytic degradation are significantly higher, and their associated peaks become more intense than the T_g values of original PET MPs. This phenomenon has been reported earlier and is attributed to the relaxation process of the amorphous region of PET MPs resulting from the mobility of the molecules segments (Farhoodi et al., 2012). Meanwhile, the cold crystallization peaks, associated with the rearrangement of the amorphous phase into a crystal phase during DSC heating (Fechine et al., 2002), are slightly lower after photocatalytic degradation of PET MPs. The second thermal transition observed corresponds to the melting temperature. The obtained T_m values after photocatalytic degradation are slightly lower than the one of the original PET, which could also be attributed to the relaxation process (Aljoumaa and Abboudi, 2016).

In the cooling scan depicted in Figure 6(b), the original PET MPs showed a pronounced peak associated with the crystallization process of PET. However, the peak of the degraded MPs was considerably less intense and appeared at lower temperatures than the original MPs, as exhibited in Table 3. The decrease in T_c can be associated with branching and crosslinking reactions (Horne et al., 2020).

The degree of crystallinity calculated from Eq. 2 is also presented in Table 3. The degree of crystallinity, also known as the crystallinity index, is often used as an indicator of the degradation of PET (Hagihara et al., 2014). The degree of crystallinity obtained for the samples subjected to photocatalytic degradation at pH 6 and 8 under visible irradiation shows a marked decrease compared to original PET MPs. This effect has been reported before in literature (Fechine et al., 2002; Miranda et al., 2021; Nguyen-Tri and Prud'homme, 2019; Niaounakis et al., 2019) but is also in disagreement with other works which have reported the opposite effect (Arhant et al., 2019; Farhoodi et al., 2012). To understand this phenomenon, it is important to identify the degradation process that the polymer is going through. The most relevant degradation mechanisms of PET include photo-oxidation, thermal and hydrolytic degradation (Fotopoulou and Karapanagioti, 2017).

In this work, the main pathways for degradation of PET MPs are hydrolysis, as the experiments are performed in an aquatic environment and visible light-induced photo-oxidation. During the photo-oxidation of PET, it is expected that a chemi-crystallization process will occur. This process consists of the reorganization of the amorphous phase into a crystalline phase because of the chain scission during degradation, leading to an increase in crystallinity (Arhant

et al., 2019; Fechine et al., 2002). Since the rearrangement of the molecules depends on their mobility, it is expected that the chemi-crystallization process occurs only at temperatures higher than the glass transition temperature (T_g) (Fechine et al., 2002). However, it has been proven that the chemi-crystallization process can occur even at temperatures below the T_g if the environment contains moisture, as the water can act as a plasticizer, promoting molecular mobility (Fechine et al., 2002). This process is known as hydrolysis. During the hydrolysis process, carboxylic and hydroxyl end groups are formed, leading to the breakdown of water-activated ester bonds, resulting in the cleavage of polymer chains (Mendiburu-Valor et al., 2022). Hydrolysis occurs when the water diffuses into the amorphous regions of the polymer, leaving the crystalline regions untouched because of its impermeability to water (Fotopoulou and Karapanagioti, 2017; Sang et al., 2020) and therefore increasing the crystallinity of PET. Nonetheless, as indicated earlier, a decrease in crystallinity in which photolysis and hydrolysis were the main degradation mechanisms, as investigated in this work, has been reported by several works (Gardette et al., 2014; Miranda et al., 2021; Nguyen-Tri and Prud'homme, 2019; Niaounakis et al., 2019). An explanation could be that PET absorbs light causing chain scission within its crystalline regions, resulting in a decrease of crystallinity, but further research is needed to determine the factors that promote one degradation pathway over the other when hydrolytic degradation and photo-oxidation are combined (Sang et al., 2020).

Thermogravimetric analysis was used to study the effect of visible light photocatalytic degradation on the thermal stability of PET MPs at different pH. The thermal curves are presented in Figure 6(c). and the T_{onset} temperatures for

each condition are shown in Table 3. The original PET MPs present good thermostability until around 350 °C when thermal degradation occurs. However, PET MPs that underwent a photocatalytic degradation process showed a decrease in the degradation temperature and T_{onset}. This is attributed to the chain scission resulting from photocatalytic degradation, causing a decline in the molar mass and embrittlement of the polymer chain, reducing the thermal stability of the PET MPs (Lee et al., 2012; Pires et al., 2015). All the samples exhibited a two-step thermal degradation. The primary step occurs between 300 – 450 °C and corresponds to the ester linkage decomposition due to chain scission, generating vinyl- and carboxy-terminated chain fragments (Achagri et al., 2020). The secondary step starts at 600 °C and corresponds to C-C bonds cleavage, forming volatile compounds (Achagri et al., 2020).

Table 3. Thermal properties of PET MPs before and after photocatalytic degradation

Sample	Heating				Cooling		T_{onset} (°C)
	T_g (°C)	T_{cc} (°C)	T_m (°C)	X_c (%)	T_c (°C)	X_c (%)	
PET Original	73.0	129.0	254.0	9.1	206.0	28.5	418.0
PET, TS-ME/pH 6	83.0	129.1	253.1	5.3	203.1	21.3	407.6
PET, TS-MG/pH 6	79.0	128.8	251.6	5.7	203.2	22.8	403.4
PET, TS-ME/pH 8	79.8	128.3	251.1	4.9	204.0	17.3	406.4
PET, TS-MG/pH 8	82.0	127.8	250.4	2.8	200.1	10.8	405.1

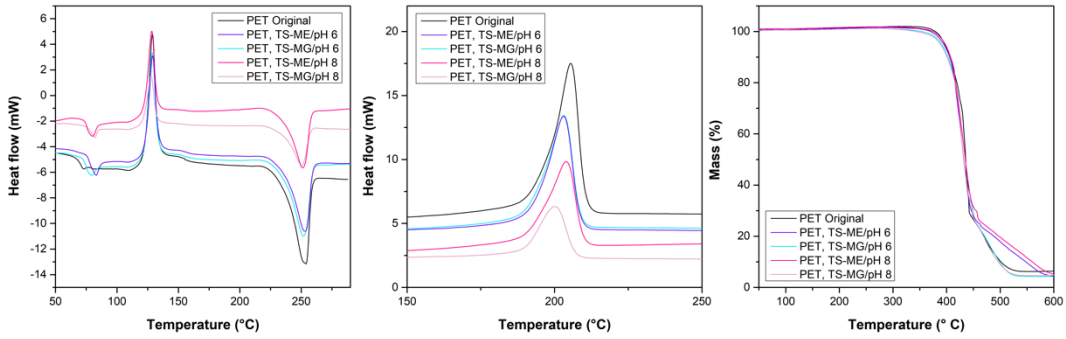

Figure 6. (a) DSC heating scans, (b) DSC cooling scans, and (c) TGA weight loss curves of different PET MPs samples.

SEM micrographs of the PET MPs were taken to investigate the changes in morphology due to photocatalytic degradation. For this study, PET MPs were obtained from the grinding of a PET food container, leaving cuts on the surface of the samples because of the use of blades in the fragmentation process, which would limit the analysis of the samples using SEM. Therefore, we analyzed the samples from the surfaces that were not cut by the blades and remained intact. As can be noted from Figure 7, the original PET MPs exhibit a uniform flat surface, which was not significantly altered after the photolysis. However, after the PET microplastics were exposed to a photocatalytic treatment using TS-ME and TS-MG photocatalysts and pH 6 and 8, holes and cracks were formed on their surface due to degradation (Horne et al., 2020).

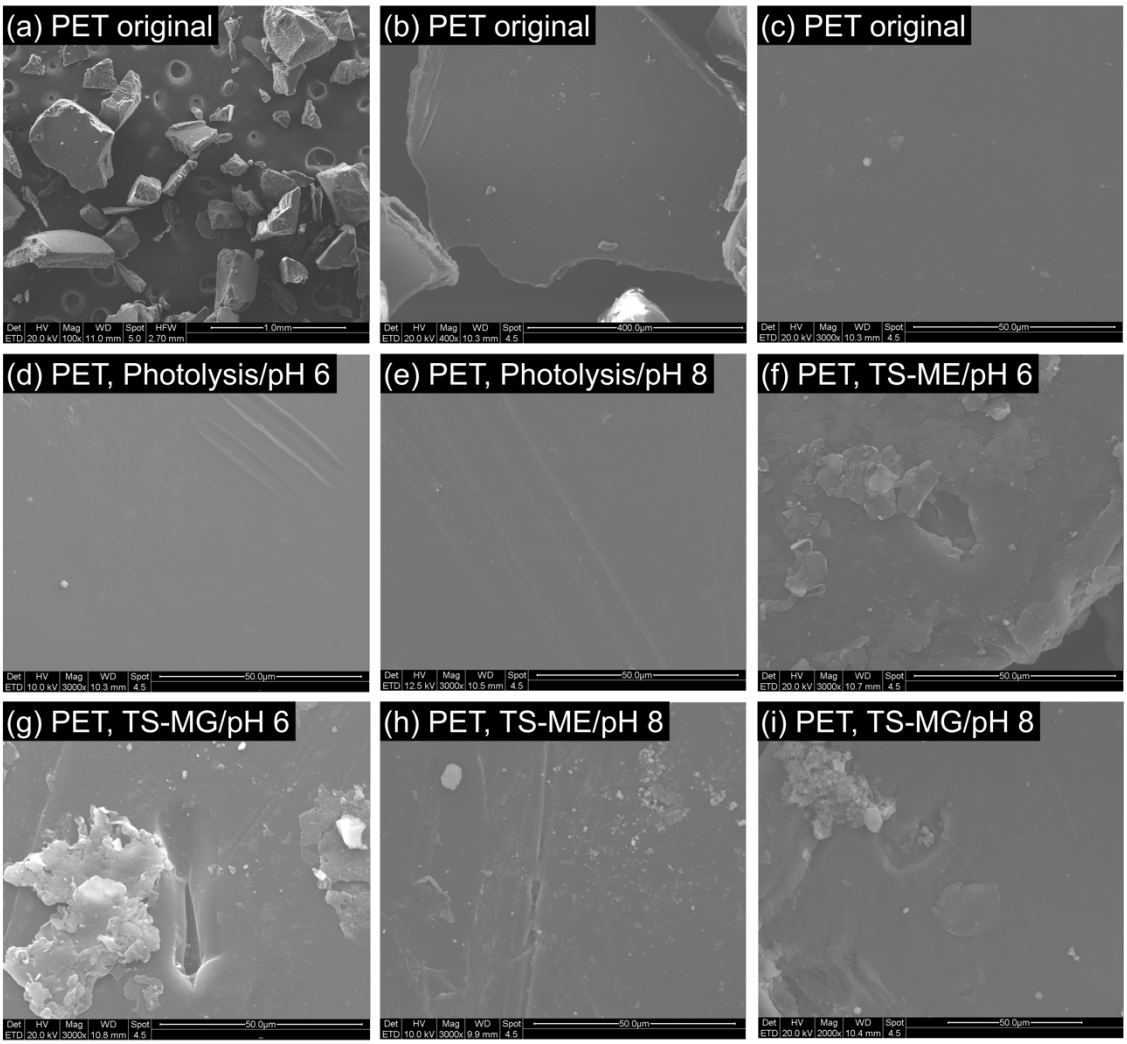

Figure 7. SEM micrographs of PET MPs (a)-(c) before photocatalytic degradation; (d)-(e) after photolysis; (f)-(i) after 120 h of irradiation with different photocatalysts and pH.

4. Conclusions

This work conducted a photocatalytic degradation using novel protein-based C,N-TiO_2/SiO_2 photocatalysts. It was demonstrated that the photocatalysts have optimal photon absorption and surface area properties, making them suitable to work in a wide range of the electromagnetic spectrum and degrade various contaminants, including PET MPs. Analysis of the conducted experiments' mass loss and carbonyl index revealed the possibility of degrading fragments of PET size ≤500 μm in ambient temperature conditions and pH 6 and 8. According to the obtained results, there is no significant difference in the photocatalytic activity of C,N-TiO_2/SiO_2 photocatalysts if they are synthesized using *Mytilus edulis* or *Mytilus galloprovincialis* extrapallial fluid as a source of carbon and nitrogen doping. This is an outstanding achievement as this synthesis can be performed in different parts of the world where these species are found, and the results would be similar. Also, results indicate that the main degradation mechanisms of PET MPs were photo-oxidation and hydrolysis. As PET MPs were predominantly amorphous, the degradation was improved as the hydrolysis occurred in the amorphous region of the polymer, which was also boosted by the slightly acidic and alkaline conditions. Nonetheless, further research is needed to thoroughly understand the mechanism of hydrolytic degradation and the changes in crystallinity when the main mechanisms are photo-oxidation and hydrolysis.

CRediT authorship contribution statement

Maria Camila Ariza-Tarazona: Methodology, Investigation, Formal Analysis, Writing – Original Draft, Writing - Review & Editing **Cristina Siligardi:** Writing - Review & Editing, Supervision, Resources **Hugo Alejandro Carreón-López:** Investigation **José Enrique Valdéz-Cerda:** Supervision, **Paolo Pozzi:** Resources **Garima Kaushik:** Resources, Writing - Review & Editing **Juan Francisco Villarreal-Chiu:** Methodology, Review & Editing, Supervision **Erika Iveth Cedillo-González:** Conceptualization, Methodology, Investigation, Writing – Original Draft, Writing - Review & Editing, Supervision, Project administration, Funding acquisition.

Declaration of Competing Interest

The authors declare no competing financial interest.

Data Availability

The data that support the findings of this study are available from the corresponding authors (MCAT, EICG), upon reasonable request.

Acknowledgments

This work was partially supported by CONACYT [Grant APN-2017/5167].

References

Achagri, G., Essamlali, Y., Amadine, O., Majdoub, M., Chakir, A., Zahouily, M., 2020. Surface modification of highly hydrophobic polyester fabric coated with octadecylamine-functionalized graphene nanosheets. RSC Adv. 10, 24941–24950. https://doi.org/10.1039/D0RA02655G

Aljoumaa, K., Abboudi, M., 2016. Physical ageing of polyethylene terephthalate under natural sunlight: correlation study between crystallinity and mechanical properties. Appl. Phys. A 122, 6. https://doi.org/10.1007/s00339-015-9518-0

Allen, N.S., Edge, M., Mohammadian, M., Jones, K., 1994. Physicochemical aspects of the environmental degradation of poly(ethylene terephthalate). Polymer Degradation and Stability 43, 229–237. https://doi.org/10.1016/0141-3910(94)90074-4

Allen, S., Allen, D., Moss, K., Le Roux, G., Phoenix, V.R., Sonke, J.E., 2020. Examination of the ocean as a source for atmospheric microplastics. PLoS ONE 15, e0232746. https://doi.org/10.1371/journal.pone.0232746

Aman, N., Das, N.N., Mishra, T., 2016. Effect of N-doping on visible light activity of TiO_2 –SiO_2 mixed oxide photocatalysts. Journal of Environmental Chemical Engineering 4, 191–196. https://doi.org/10.1016/j.jece.2015.10.037

Ang, T.P., Toh, C.S., Han, Y.-F., 2009. Synthesis, Characterization, and Activity of Visible-Light-Driven Nitrogen-Doped TiO_2 −SiO_2 Mixed Oxide Photocatalysts. J. Phys. Chem. C 113, 10560–10567. https://doi.org/10.1021/jp9000658

Arhant, M., Le Gall, M., Le Gac, P.-Y., Davies, P., 2019. Impact of hydrolytic degradation on mechanical properties of PET - Towards an understanding of

586 microplastics formation. Polymer Degradation and Stability 161, 175–182.
587 https://doi.org/10.1016/j.polymdegradstab.2019.01.021
588 Ariza-Tarazona, M.C., Villarreal-Chiu, J.F., Barbieri, V., Siligardi, C., Cedillo-González,
589 E.I., 2019. New strategy for microplastic degradation: Green photocatalysis
590 using a protein-based porous N-TiO_2 semiconductor. Ceramics International, A
591 selection of papers presented at CIMTEC 2018 45, 9618–9624.
592 https://doi.org/10.1016/j.ceramint.2018.10.208
593 Ariza-Tarazona, M.C., Villarreal-Chiu, J.F., Hernández-López, J.M., Rivera De la Rosa,
594 J., Barbieri, V., Siligardi, C., Cedillo-González, E.I., 2020. Microplastic pollution
595 reduction by a carbon and nitrogen-doped TiO_2: Effect of pH and temperature in
596 the photocatalytic degradation process. Journal of Hazardous Materials 395,
597 122632. https://doi.org/10.1016/j.jhazmat.2020.122632
598 Barceló, D., Picó, Y., 2019. Microplastics in the global aquatic environment: Analysis,
599 effects, remediation and policy solutions. Journal of Environmental Chemical
600 Engineering 7, 103421. https://doi.org/10.1016/j.jece.2019.103421
601 Bertoldo, M., Labardi, M., Rotella, C., Capaccioli, S., 2010. Enhanced crystallization
602 kinetics in poly(ethylene terephthalate) thin films evidenced by infrared
603 spectroscopy. Polymer 51, 3660–3668.
604 https://doi.org/10.1016/j.polymer.2010.05.040
605 Bond, T., Ferrandiz-Mas, V., Felipe-Sotelo, M., van Sebille, E., 2018. The occurrence
606 and degradation of aquatic plastic litter based on polymer physicochemical
607 properties: A review. Critical Reviews in Environmental Science and
608 Technology 48, 685–722. https://doi.org/10.1080/10643389.2018.1483155
609 Brahney, J., Mahowald, N., Prank, M., Cornwell, G., Klimont, Z., Matsui, H., Prather,
610 K.A., 2021. Constraining the atmospheric limb of the plastic cycle. Proceedings
611 of the National Academy of Sciences of the United States of America 118.
612 https://doi.org/10.1073/pnas.2020719118
613 Chamas, A., Moon, H., Zheng, J., Qiu, Y., Tabassum, T., Jang, J.H., Abu-Omar, M.,
614 Scott, S.L., Suh, S., 2020. Degradation Rates of Plastics in the Environment.
615 ACS Sustainable Chem. Eng. 8, 3494–3511.
616 https://doi.org/10.1021/acssuschemeng.9b06635
617 Cole, K.C., Ajji, A., Pellerin, É., 2002. New Insights into the Development of Ordered
618 Structure in Poly(ethylene terephthalate). 1. Results from External Reflection
619 Infrared Spectroscopy. Macromolecules 35, 770–784.
620 https://doi.org/10.1021/ma011492i
621 Edge, M., Hayes, M., Mohammadian, M., Allen, N.S., Jewitt, T.S., Brems, K., Jones, K.,
622 1991. Aspects of poly(ethylene terephthalate) degradation for archival life and
623 environmental degradation. Polymer Degradation and Stability 32, 131–153.
624 https://doi.org/10.1016/0141-3910(91)90047-U
625 Farhoodi, M., Mousavi, S.M., Sotudeh-Gharebagh, R., Emam-Djomeh, Z., Oromiehie,
626 A., Mansour, H., 2012. A Study on Physical Aging of Semicrystalline
627 Polyethylene Terephthalate below the Glass Transition Point. JART 10.
628 https://doi.org/10.22201/icat.16656423.2012.10.5.360
629 Fechine, G.J.M., Souto-Maior, R.M., Rabello, M.S., 2002. Structural changes during
630 photodegradation of poly(ethylene terephthalate). Journal of Materials Science
631 37, 4979–4984. https://doi.org/10.1023/A:1021067027612
632 Ferreira, M.M., da Silva, E.A., Cotting, F., Lins, V. de F.C., 2021. UV weathering and
633 performance of a novel corrosion protective coating on steel made from
634 recycled polyethylene terephthalate (PET). Corrosion Engineering, Science and
635 Technology 56, 199–209. https://doi.org/10.1080/1478422X.2020.1836880
636 Fotopoulou, K.N., Karapanagioti, H.K., 2017. Degradation of Various Plastics in the
637 Environment, in: Takada, H., Karapanagioti, H.K. (Eds.), Hazardous Chemicals
638 Associated with Plastics in the Marine Environment, The Handbook of
639 Environmental Chemistry. Springer International Publishing, Cham, pp. 71–92.
640 https://doi.org/10.1007/698_2017_11

641 Gao, F., Li, J., Sun, C., Zhang, L., Jiang, F., Cao, W., Zheng, L., 2019. Study on the
642 capability and characteristics of heavy metals enriched on microplastics in
643 marine environment. Marine Pollution Bulletin 144, 61–67.
644 https://doi.org/10.1016/j.marpolbul.2019.04.039
645 Gardette, J.-L., Colin, A., Trivis, S., German, S., Therias, S., 2014. Impact of photo-
646 oxidative degradation on the oxygen permeability of
647 poly(ethyleneterephthalate). Polymer Degradation and Stability 103, 35–41.
648 https://doi.org/10.1016/j.polymdegradstab.2014.02.021
649 Guo, N., Liang, Y., Lan, S., Liu, L., Ji, G., Gan, S., Zou, H., Xu, X., 2014. Uniform
650 TiO2–SiO2 hollow nanospheres: Synthesis, characterization and enhanced
651 adsorption–photodegradation of azo dyes and phenol. Applied Surface Science
652 305, 562–574. https://doi.org/10.1016/j.apsusc.2014.03.136
653 Hagihara, H., Oishi, A., Funabashi, M., Kunioka, M., Suda, H., 2014. Free-volume hole
654 size evaluated by positron annihilation lifetime spectroscopy in the amorphous
655 part of poly(ethylene terephthalate) degraded by a weathering test. Polymer
656 Degradation and Stability 110, 389–394.
657 https://doi.org/10.1016/j.polymdegradstab.2014.10.008
658 Hale, R.C., Seeley, M.E., La Guardia, M.J., Mai, L., Zeng, E.Y., 2020. A Global
659 Perspective on Microplastics. Journal of Geophysical Research: Oceans 125,
660 e2018JC014719. https://doi.org/10.1029/2018JC014719
661 Horne, F.J., Liggat, J.J., MacDonald, W.A., Sankey, S.W., 2020. Photo-oxidation of
662 poly(ethylene terephthalate) films intended for photovoltaic backsheet. Journal
663 of Applied Polymer Science 137, 48623. https://doi.org/10.1002/app.48623
664 Ioakeimidis, C., Fotopoulou, K.N., Karapanagioti, H.K., Geraga, M., Zeri, C.,
665 Papathanassiou, E., Galgani, F., Papatheodorou, G., 2016. The degradation
666 potential of PET bottles in the marine environment: An ATR-FTIR based
667 approach. Sci Rep 6, 23501. https://doi.org/10.1038/srep23501
668 Janczak, K., Dąbrowska, G.B., Raszkowska-Kaczor, A., Kaczor, D., Hrynkiewicz, K.,
669 Richert, A., 2020. Biodegradation of the plastics PLA and PET in cultivated soil
670 with the participation of microorganisms and plants. International
671 Biodeterioration & Biodegradation 155, 105087.
672 https://doi.org/10.1016/j.ibiod.2020.105087
673 Jiang, R., Lu, G., Yan, Z., Liu, J., Wu, D., Wang, Y., 2021. Microplastic degradation by
674 hydroxy-rich bismuth oxychloride. Journal of Hazardous Materials 405, 124247.
675 https://doi.org/10.1016/j.jhazmat.2020.124247
676 Jiménez-González, C., Constable, D.J.C., 2011. Green Chemistry and Engineering: A
677 Practical Design Approach. John Wiley & Sons.
678 Koelmans, A.A., Bakir, A., Burton, G.A., Janssen, C.R., 2016. Microplastic as a Vector
679 for Chemicals in the Aquatic Environment: Critical Review and Model-
680 Supported Reinterpretation of Empirical Studies. Environ. Sci. Technol. 50,
681 3315–3326. https://doi.org/10.1021/acs.est.5b06069
682 Kong, Y., Hay, J.N., 2002. The measurement of the crystallinity of polymers by DSC.
683 Polymer 43, 3873–3878. https://doi.org/10.1016/S0032-3861(02)00235-5
684 Lee, C.O., Chae, B., Kim, S.B., Jung, Y.M., Lee, S.W., 2012. Two-dimensional
685 correlation analysis study of the photo-degradation of poly(ethylene
686 terephthalate) film. Vibrational Spectroscopy 60, 142–145.
687 https://doi.org/10.1016/j.vibspec.2011.10.013
688 Loaeza, D., Cailloux, J., Santana Pérez, O., Sánchez-Soto, M., Maspoch, M., 2021.
689 Impact of Titanium Dioxide in the Mechanical Recycling of Post-Consumer
690 Polyethylene Terephthalate Bottle Waste: Tensile and Fracture Behavior.
691 Polymers 13, 310. https://doi.org/10.3390/polym13020310
692 Magalhães, S., Alves, L., Medronho, B., Romano, A., Rasteiro, M. da G., 2020.
693 Microplastics in Ecosystems: From Current Trends to Bio-Based Removal
694 Strategies. Molecules 25, 3954. https://doi.org/10.3390/molecules25173954

695 Mendiburu-Valor, E., Mondragon, G., González, N., Kortaberria, G., Martin, L., Eceiza,
696 A., Peña-Rodriguez, C., 2022. Valorization of urban and marine PET waste by
697 optimized chemical recycling. Resources, Conservation and Recycling 184,
698 106413. https://doi.org/10.1016/j.resconrec.2022.106413
699 Miranda, M.N., Sampaio, M.J., Tavares, P.B., Silva, A.M.T., Pereira, M.F.R., 2021.
700 Aging assessment of microplastics (LDPE, PET and uPVC) under urban
701 environment stressors. Science of The Total Environment 796, 148914.
702 https://doi.org/10.1016/j.scitotenv.2021.148914
703 Mueller, R.-J., 2006. Biological degradation of synthetic polyesters—Enzymes as
704 potential catalysts for polyester recycling. Process Biochemistry, From
705 Biochemical Engineering to Systems Biology 41, 2124–2128.
706 https://doi.org/10.1016/j.procbio.2006.05.018
707 Nguyen-Tri, P., El Aidani, R., Leborgne, É., Pham, T., Vu-Khanh, T., 2014. Chemical
708 ageingaging of a polyester nonwoven membrane used in aerosol and drainage
709 filter. Polymer Degradation and Stability 101, 71–80.
710 https://doi.org/10.1016/j.polymdegradstab.2014.01.001
711 Nguyen-Tri, P., Prud'homme, R.E., 2019. Nanoscale analysis of the photodegradation
712 of polyester fibers by AFM-IR. Journal of Photochemistry and Photobiology A:
713 Chemistry 371, 196–204. https://doi.org/10.1016/j.jphotochem.2018.11.017
714 Niaounakis, M., Kontou, E., Pispas, S., Kafetzi, M., Giaouzi, D., 2019. Aging of
715 packaging films in the marine environment. Polym Eng Sci 59, E432–E441.
716 https://doi.org/10.1002/pen.25079
717 Piccardo, M., Provenza, F., Grazioli, E., Cavallo, A., Terlizzi, A., Renzi, M., 2020. PET
718 microplastics toxicity on marine key species is influenced by pH, particle size
719 and food variations. Science of The Total Environment 715, 136947.
720 https://doi.org/10.1016/j.scitotenv.2020.136947
721 Pires, H.M., Mendes, L.C., Cestari, S.P., Pita, V.J.R.R., 2015. Effect of Weathering and
722 Accelerated Photoaging on PET/PC (80/20 wt/wt%) Melt Extruded Blend. Mat.
723 Res. 18, 763–768. https://doi.org/10.1590/1516-1439.010115
724 Ragusa, A., Svelato, A., Santacroce, C., Catalano, P., Notarstefano, V., Carnevali, O.,
725 Papa, F., Rongioletti, M.C.A., Baiocco, F., Draghi, S., D'Amore, E., Rinaldo, D.,
726 Matta, M., Giorgini, E., 2021. Plasticenta: First evidence of microplastics in
727 human placenta. Environment International 146, 106274.
728 https://doi.org/10.1016/j.envint.2020.106274
729 Rouillon, C., Bussiere, P.-O., Desnoux, E., Collin, S., Vial, C., Therias, S., Gardette, J.-
730 L., 2016. Is carbonyl index a quantitative probe to monitor polypropylene
731 photodegradation? Polymer Degradation and Stability 128, 200–208.
732 https://doi.org/10.1016/j.polymdegradstab.2015.12.011
733 Sang, T., Wallis, C.J., Hill, G., Britovsek, G.J.P., 2020. Polyethylene terephthalate
734 degradation under natural and accelerated weathering conditions. European
735 Polymer Journal 136, 109873. https://doi.org/10.1016/j.eurpolymj.2020.109873
736 Schwabl, P., Köppel, S., Königshofer, P., Bucsics, T., Trauner, M., Reiberger, T.,
737 Liebmann, B., 2019. Detection of Various Microplastics in Human Stool. Ann
738 Intern Med 171, 453–457. https://doi.org/10.7326/M19-0618
739 Sharma, S., Basu, S., Shetti, N.P., Nadagouda, M.N., Aminabhavi, T.M., 2020.
740 Microplastics in the environment: occurrence, perils, and eradication. Chemical
741 Engineering Journal 127317. https://doi.org/10.1016/j.cej.2020.127317
742 Uheida, A., Mejía, H.G., Abdel-Rehim, M., Hamd, W., Dutta, J., 2021. Visible light
743 photocatalytic degradation of polypropylene microplastics in a continuous water
744 flow system. Journal of Hazardous Materials 406, 124299.
745 https://doi.org/10.1016/j.jhazmat.2020.124299
746 Wang, C., Zhao, J., Xing, B., 2021. Environmental source, fate, and toxicity of
747 microplastics. Journal of Hazardous Materials 407, 124357.
748 https://doi.org/10.1016/j.jhazmat.2020.124357

Zeng, H., Xie, J., Xie, H., Su, B.-L., Wang, M., Ping, H., Wang, W., Wang, H., Fu, Z., 2015. Bioprocess-inspired synthesis of hierarchically porous nitrogen-doped TiO_2 with high visible-light photocatalytic activity. J. Mater. Chem. A 3, 19588–19596. https://doi.org/10.1039/C5TA04649A

Zhang, K., Hamidian, A.H., Tubić, A., Zhang, Y., Fang, J.K.H., Wu, C., Lam, P.K.S., 2021. Understanding plastic degradation and microplastic formation in the environment: A review. Environmental Pollution 274, 116554. https://doi.org/10.1016/j.envpol.2021.116554

Zhang, W., Zhang, Y., Yang, K., Yang, Y., Jia, J., Guo, L., 2019. Photocatalytic Performance of SiO_2/CNOs/TiO_2 to Accelerate the Degradation of Rhodamine B under Visible Light. Nanomaterials 9, 1671. https://doi.org/10.3390/nano9121671

Zhou, D., Luo, H., Zhang, F., Wu, J., Yang, J., Wang, H., 2022a. Efficient Photocatalytic Degradation of the Persistent PET Fiber-Based Microplastics over Pt Nanoparticles Decorated N-Doped TiO_2 Nanoflowers. Advanced Fiber Materials 1–14. https://doi.org/10.1007/s42765-022-00149-4

Zhou, D., Wang, L., Zhang, F., Wu, J., Wang, H., Yang, J., 2022b. Feasible Degradation of Polyethylene Terephthalate Fiber-Based Microplastics in Alkaline Media with Bi_2O_3@ N-TiO_2 Z-Scheme Photocatalytic System. Advanced Sustainable Systems 6, 2100516. https://doi.org/10.1002/adsu.202100516

Supplementary Information

Low Environmental Impact Remediation of Microplastics: Visible-Light Photocatalytic Degradation of PET Microplastics Using Bio-Inspired C,N-TiO_2/SiO_2 Photocatalysts

Maria Camila Ariza-Tarazona[a,b*], Cristina Siligardi[a,b], Hugo Alejandro Carreón-López[c], José Enrique Valdéz-Cerda[c], Paolo Pozzi[a], Garima Kaushik[e] , Juan Francisco Villarreal-Chiu[c,d], Erika Iveth Cedillo-González[a,b*]

[a]Department of Engineering “Enzo Ferrari”, University of Modena and Reggio Emilia, Via P. Vivarelli 10/1, Modena, 41125, Italy.

[b]National Interuniversity Consortium of Materials Science and Technology (INSTM), Via Giusti, Florence, 50121, Italy

[c]Universidad Autónoma de Nuevo León, Facultad de Ciencias Químicas. Av. Universidad S/N Ciudad Universitaria, San Nicolás de los Garza, 66455, Nuevo León, México.

[d]Centro de Investigación en Biotecnología y Nanotecnología (CIByN), Facultad de Ciencias Químicas, Universidad Autónoma de Nuevo León. Parque de Investigación e Innovación Tecnológica, Km. 10 autopista al Aeropuerto Internacional Mariano Escobedo, Apodaca, 66628, Nuevo León, México.
[e]Department of Environmental Science, School of Earth Sciences, Central University of Rajasthan, Ajmer 305817, India
[*]***Corresponding author***
E-mail adresses: mariacamila.arizatarazona@unimore.it (M. C. Ariza-Tarazona), ecedillo@unimore.it (E.I. Cedillo-González)

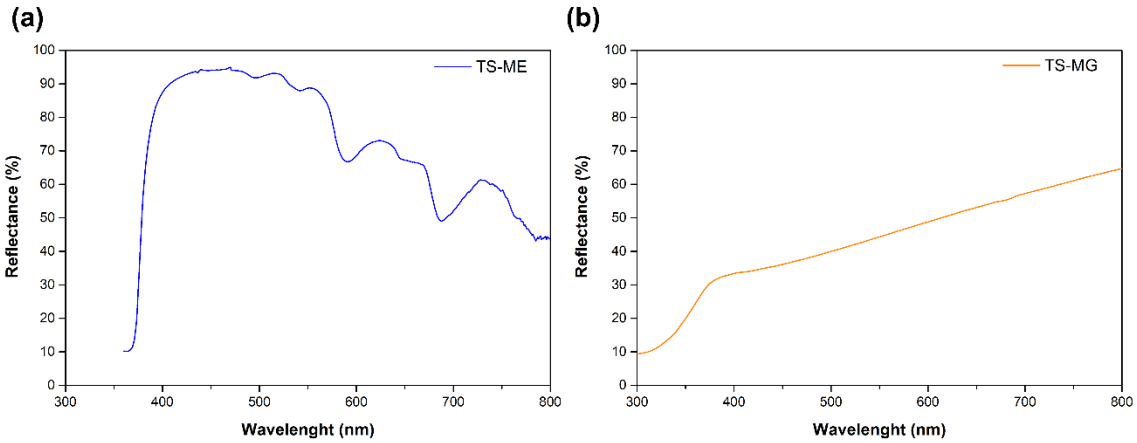

Fig 1S. Absorbance spectra of C,N-TiO_2/SiO_2 samples.

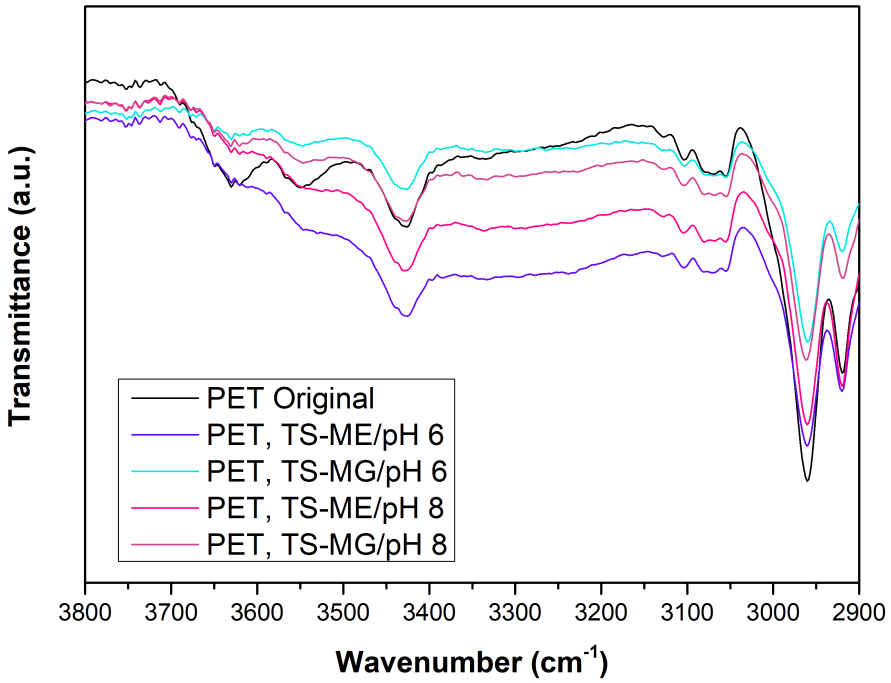

802 **Fig 2S.** ATR-FTIR of PET MPs in the range from 3800 to 2900 cm^{-1}.

803

804

805